The Astronomical Journal, 159:98 (13pp), 2020 March https://doi.org/10.3847/1538-3881/ab660e

KMT-2016-BLG-1836Lb: A Super-Jovian Planet from a High-cadence Microlensing Field

Hongjing Yang[1,2], Xiangyu Zhang[1], Kyu-Ha Hwang[3], Weicheng Zang[1], Andrew Gould[4,5], Tianshu Wang[1], Shude Mao[1,6], Michael D. Albrow[7], Sun-Ju Chung[3,8], Cheongho Han[9], Youn Kil Jung[3], Yoon-Hyun Ryu[3], In-Gu Shin[3], Yossi Shvartzvald[10], Jennifer C. Yee[11], Wei Zhu[12], Matthew T. Penny[13], Pascal Fouqué[14,15], Sang-Mok Cha[3,16], Dong-Jin Kim[3], Hyoun-Woo Kim[3], Seung-Lee Kim[3,8], Chung-Uk Lee[3,8], Dong-Joo Lee[3], Yongseok Lee[3,16], Byeong-Gon Park[3,17], and Richard W. Pogge[5]

[1] Department of Astronomy and Tsinghua Centre for Astrophysics, Tsinghua University, Beijing 100084, People's Republic of China
zangwc17@mails.tsinghua.edu.cn
[2] Department of Astronomy, Xiamen University, Xiamen 361005, People's Republic of China
[3] Korea Astronomy and Space Science Institute, Daejon 34055, Republic of Korea
[4] Max-Planck-Institute for Astronomy, Königstuhl 17, D-69117 Heidelberg, Germany
[5] Department of Astronomy, Ohio State University, 140 W. 18th Avenue, Columbus, OH 43210, USA
[6] National Astronomical Observatories, Chinese Academy of Sciences, Beijing 100101, People's Republic of China
[7] University of Canterbury, Department of Physics and Astronomy, Private Bag 4800, Christchurch 8020, New Zealand
[8] University of Science and Technology, Korea, (UST), 217 Gajeong-ro Yuseong-gu, Daejeon 34113, Republic of Korea
[9] Department of Physics, Chungbuk National University, Cheongju 28644, Republic of Korea
[10] IPAC, Mail Code 100-22, Caltech, 1200 E. California Boulevard, Pasadena, CA 91125, USA
[11] Center for Astrophysics | Harvard & Smithsonian, 60 Garden Street, Cambridge, MA 02138, USA
[12] Canadian Institute for Theoretical Astrophysics, University of Toronto, 60 St. George Street, Toronto, ON M5S 3H8, Canada
[13] Department of Astronomy, The Ohio State University, 140 W. 18th Avenue, Columbus, OH 43210, USA
[14] CFHT Corporation, 65-1238 Mamalahoa Hwy, Kamuela, HI 96743, USA
[15] Université de Toulouse, UPS-OMP, IRAP, Toulouse, France
[16] School of Space Research, Kyung Hee University, Yongin, Kyeonggi 17104, Republic of Korea
[17] Korea University of Science and Technology, 217 Gajeong-ro, Yuseong-gu, Daejeon 34113, Republic of Korea
Received 2019 August 27; revised 2019 December 21; accepted 2019 December 26; published 2020 February 11

Abstract

We report the discovery of a super-Jovian planet in the microlensing event KMT-2016-BLG-1836, which was found by the Korea Microlensing Telescope Network (KMTNet) high-cadence observations ($\Gamma \sim 4\ \mathrm{hr}^{-1}$). The planet–host mass ratio $q \sim 0.004$. A Bayesian analysis indicates that the planetary system is composed of a super-Jovian $M_{\rm planet} = 2.2^{+1.9}_{-1.1} M_{\rm J}$ planet orbiting an M or K dwarf, $M_{\rm host} = 0.49^{+0.38}_{-0.25} M_{\odot}$, at a distance of $D_{\rm L} = 7.1^{+0.8}_{-2.4}$ kpc. The projected planet–host separation is $3.5^{+1.1}_{-0.9}$ au, implying that the planet is located beyond the snow line of the host star. Future high-resolution images can potentially strongly constrain the lens brightness and thus the mass and distance of the planetary system. Without considering detailed detection efficiency, selection, or publication biases, we find a potential mass-ratio desert at $-3.7 \lesssim \log q \lesssim -3.0$ for the 31 published KMTNet planets.

Unified Astronomy Thesaurus concepts: Gravitational microlensing exoplanet detection (2147)

Supporting material: data behind figure

1. Introduction

Since the first robust detection of a microlens planet in 2003 (Bond et al. 2004), more than 70[18] extrasolar planets have been detected by the microlensing method (Mao & Paczynski 1991; Gould & Loeb 1992). Unlike other methods that rely on the light from the host stars, the microlensing method uses the light from a background source deflected by the gravitational potential of an aligned foreground planetary system. Thus, microlensing can detect planets around all types of stellar objects at various Galactocentric distances (e.g., Calchi Novati et al. 2015; Zhu et al. 2017).

The typical Einstein timescale $t_{\rm E}$ for microlensing events is about 20 days, and the half-duration of a planetary perturbation (Gould & Loeb 1992) is

$$t_p \sim t_{\rm E}\sqrt{q} \rightarrow 5(q/10^{-4})^{1/2}\ \mathrm{hr}, \tag{1}$$

where q is the planet–host mass ratio. Assuming that about 10 data points are needed to cover the planetary perturbation, a cadence of $\Gamma \sim 1\ \mathrm{hr}^{-1}$ would be required to discover Neptunes and $\Gamma \sim 4\ \mathrm{hr}^{-1}$ would be required to detect Earths (Henderson et al. 2014). In addition, because the optical depth to microlensing toward the Galactic bulge is only $\tau \sim 10^{-6}$ (Sumi et al. 2013; Mróz et al. 2019), a large area (10–100 deg^2) must be monitored to find a large number of microlensing events and thus planetary events.

For many years, most microlensing planets were discovered by a combination of wide-area surveys for finding microlensing events and intensive follow-up observations for capturing the planetary perturbation (Gould & Loeb 1992). This strategy mainly focused on high-magnification events (e.g., Udalski et al. 2005), which intrinsically have high sensitivity to planets (Griest & Safizadeh 1998). Another strategy to find microlensing planets is to conduct wide-area, high-cadence surveys toward the Galactic bulge. The Korea Microlensing Telescope Network (KMTNet; Kim et al. 2016) continuously monitors a broad area at relatively high-cadence toward the Galactic bulge from three 1.6 m telescopes equipped with 4 deg^2 field-of-view (FOV) cameras at the Cerro Tololo

[18] http://exoplanetarchive.ipac.caltech.edu, as of 2019 July 17.

Inter-American Observatory (CTIO) in Chile (KMTC), the South African Astronomical Observatory (SAAO) in South Africa (KMTS), and the Siding Spring Observatory (SSO) in Australia (KMTA). It aims to simultaneously find microlensing events and characterize the planetary perturbation without the need for follow-up observations.

In its 2015 commissioning season, KMTNet followed this strategy and observed four fields at a very high cadence of $\Gamma = 6\ \mathrm{hr}^{-1}$. Beginning in 2016, KMTNet monitors a total of (3, 7, 11, 2) fields at cadences of $\Gamma \sim (4, 1, 0.4, 0.2)\ \mathrm{hr}^{-1}$. See Figure 12 of Kim et al. (2018a). This new strategy mainly aims to support the *Spitzer* microlensing campaign (Gould et al. 2013, 2014, 2015a, 2015b, 2016, 2018) and to find more planets over a much broader area. So far, this new strategy has detected 30 planets in 2016–2018[19], including an Earth-mass planet found by a cadence of $\Gamma \sim 4\ \mathrm{hr}^{-1}$ (Shvartzvald et al. 2017), and a super-Jovian planet found by a cadence of $\Gamma \sim 0.2\ \mathrm{hr}^{-1}$ (Ryu et al. 2020).

Here we report the analysis of a super-Jovian planet KMT-2016-BLG-1836Lb, which was detected by the $\Gamma \sim 4\ \mathrm{hr}^{-1}$ observations of KMTNet. The paper is structured as follows. In Section 2, we introduce the KMTNet observations of this event. We then describe the light-curve modeling process in Section 3, the properties of the microlens source in Section 4, and the physical parameters of the planetary system in Section 5. Finally, we discuss the mass-ratio distributions of 31 published KMTNet planets in Section 6.

2. Observations

KMT-2016-BLG-1836 was at equatorial coordinates $(\alpha, \delta)_{\mathrm{J2000}} = (17{:}53{:}00.08, -30{:}02{:}26.70)$, corresponding to Galactic coordinates $(\ell, b) = (-0.12, -1.95)$. It was found by applying the KMTNet event-finding algorithm (Kim et al. 2018a) to the 2016 KMTNet survey data (Kim et al. 2018b), and the apparently amplified flux of a KMTNet catalog star $I = 19.20 \pm 0.13$ derived from the OGLE-III star catalog (Szymański et al. 2011) led to the detection of this microlensing event. KMT-2016-BLG-1836 was located in two slightly offset fields, BLG02 and BLG42, with a nominal combined cadence of $\Gamma = 4\ \mathrm{hr}^{-1}$. In fact, the cadence of KMTA and KMTS was altered to $\Gamma = 6\ \mathrm{hr}^{-1}$ from April 23 to June 16 ($7501 < \mathrm{HJD}' < 7555$, $\mathrm{HJD}' = \mathrm{HJD} - 2450000$) to support the *Kepler K2*C9 campaign (Gould & Horne 2013; Henderson et al. 2016; Kim et al. 2018c). This higher cadence block came toward the end of the event and after the planetary perturbation. The majority of observations were taken in the I band, with about 10% of the KMTC images and 5% of the KMTS images taken in the V band for the color measurement of microlens sources. All data for the light-curve analyses were reduced using the pySIS software package (Albrow et al. 2009), a variant of the difference image analysis (Alard & Lupton 1998). For the source color measurement and the color–magnitude diagram (CMD), we additionally conduct pyDIA photometry for the KMTC02 data, which simultaneously yields field-star photometry on the same system as the light curve.

[19] OGLE-2016-BLG-0263Lb (Han et al. 2017a), OGLE-2016-BLG-0596Lb (Mróz et al. 2017), OGLE-2016-BLG-0613Lb (Han et al. 2017b), OGLE-2016-BLG-1067Lb (Calchi Novati et al. 2019), OGLE-2016-BLG-1190Lb (Ryu et al. 2018), OGLE-2016-BLG-1195Lb (Shvartzvald et al. 2017), OGLE-2016-BLG-1227Lb (Han et al. 2019b), KMT-2016-BLG-0212Lb (Hwang et al. 2018a), KMT-2016-BLG-1107Lb (Hwang et al. 2019), KMT-2016-BLG-1397Lb (Zang et al. 2018a), KMT-2016-BLG-1820Lb (Jung et al. 2018a), MOA-2016-BLG-319Lb (Han et al. 2018a), OGLE-2017-BLG-0173Lb (Hwang et al. 2018b), OGLE-2017-BLG-0373Lb (Skowron et al. 2018), OGLE-2017-BLG-0482Lb (Han et al. 2018b), OGLE-2017-BLG-1140Lb (Calchi Novati et al. 2018), OGLE-2017-BLG-1434Lb (Udalski et al. 2018), OGLE-2017-BLG-1522Lb (Jung et al. 2018b), KMT-2017-BLG-0165Lb (Jung et al. 2019b), KMT-2017-BLG-1038Lb (Shin et al. 2019), KMT-2017-BLG-1146Lb (Shin et al. 2019), OGLE-2018-BLG-0532Lb (Ryu et al. 2019b), OGLE-2018-BLG-0596Lb (Jung et al. 2019a), OGLE-2018-BLG-0740Lb (Han et al. 2019c), OGLE-2018-BLG-1011Lbc (Han et al. 2019a), OGLE-2018-BLG-1700Lb (Han et al. 2020), KMT-2018-BLG-0029Lb (Gould et al. 2019), KMT-2018-BLG-1292Lb (Ryu et al. 2020), and KMT-2018-BLG-1990Lb (Ryu et al. 2019a).

3. Light-curve Analysis

Figure 1 shows the KMT-2016-BLG-1836 data together with the best-fit model. The light curve shows a bump ($\mathrm{HJD}' \sim 7493$) after the peak of an otherwise normal Paczyński (1986) point-lens light curve. The bump could be a binary-lensing (2L1S) anomaly, which is generally produced by caustic-crossing (e.g., Street et al. 2016) or a cusp approach (e.g., Shvartzvald et al. 2017) of the lensed star, or the second peak of a binary-source event (1L2S), which is the superposition of two point-lens events generated by two source stars (Gaudi 1998; Han 2002). Thus, we perform both binary-lens and binary-source analyses in this section.

3.1. Binary-lens (2L1S) Modeling

A standard binary-lens model has seven parameters to calculate the magnification, $A(t)$. Three (t_0, u_0, t_{E}) of these parameters describe a point-lens event (Paczyński 1986): the time of the maximum magnification, the minimum impact parameter in units of the angular Einstein radius θ_{E}, and the Einstein radius crossing time. The next three (q, s, α) define the binary geometry: the binary mass ratio, the projected separation between the binary components normalized to the Einstein radius, and the angle between the source trajectory and the binary axis in the lens plane. The last parameter is the source radius normalized by the Einstein radius, $\rho = \theta_*/\theta_{\mathrm{E}}$. In addition, for each data set i, two flux parameters ($f_{\mathrm{S},i}$, $f_{\mathrm{B},i}$) represent the flux of the source star and the blend flux. The observed flux, $f_i(t)$, calculated from the model is

$$f_i(t) = f_{\mathrm{S},i} A(t) + f_{\mathrm{B},i}. \quad (2)$$

We locate the χ^2 minima by a searching over a grid of parameters ($\log s$, $\log q$, α). The grids consist of 21 values equally spaced between $-1 \leqslant \log s \leqslant 1$, 10 values equally spaced between $0° \leqslant \alpha < 360°$, and 51 values equally spaced between $-5 \leqslant \log q \leqslant 0$. For each set of ($\log s$, $\log q$, α), we fix $\log q$, $\log s$, $\rho = 0.001$, and free t_0, u_0, t_{E}, α. We find the minimum χ^2 by Markov Chain Monte Carlo (MCMC) χ^2 minimization using the emcee ensemble sampler (Foreman-Mackey et al. 2013). The upper panel of Figure 2 shows the χ^2 distribution in the ($\log s$, $\log q$) plane from the grid search, which indicates the distinct minima are within $-0.3 \leqslant \log s \leqslant 0.3$ and $-5 \leqslant \log q \leqslant -1$. We therefore conduct a denser grid search, which consists of 61 values equally spaced between $-0.3 \leqslant \log s \leqslant 0.3$, 10 values equally spaced between $0° \leqslant \alpha < 360°$, and 41 values equally spaced between $-5 \leqslant \log q \leqslant -1$. As a result, we find four distinct minima and label them as "A," "B," "C," and "D" in the lower panel of Figure 2. We then investigate the best-fit model with all free parameters. Table 1 shows best-fit parameters of the four solutions from the MCMC. The MCMC results show that the solution "B" is the best-fit model, while the solution "A" is disfavored by $\Delta\chi^2 \sim 16$.

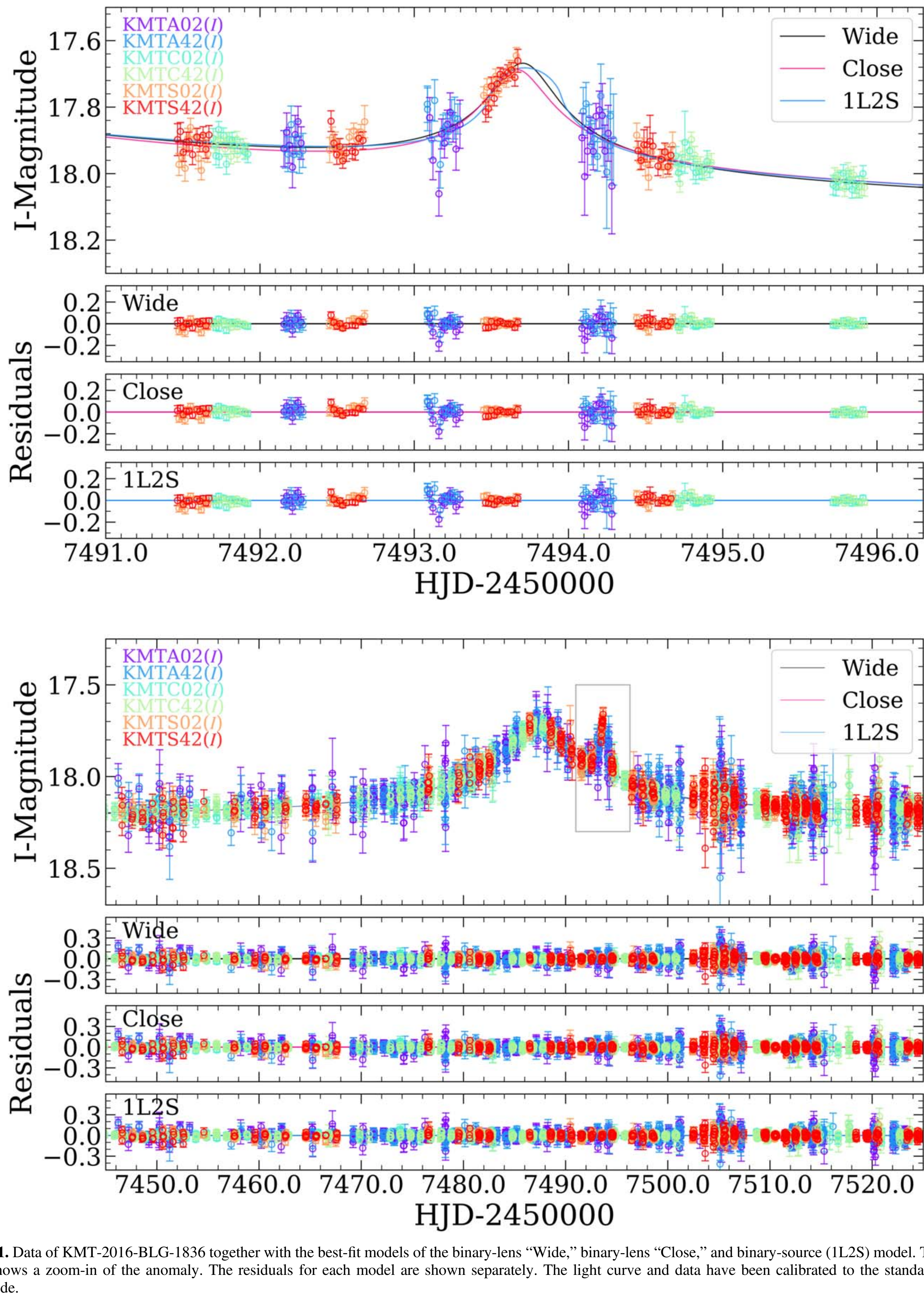

Figure 1. Data of KMT-2016-BLG-1836 together with the best-fit models of the binary-lens "Wide," binary-lens "Close," and binary-source (1L2S) model. The upper panel shows a zoom-in of the anomaly. The residuals for each model are shown separately. The light curve and data have been calibrated to the standard *I*-band magnitude.

(The data used to create this figure are available.)

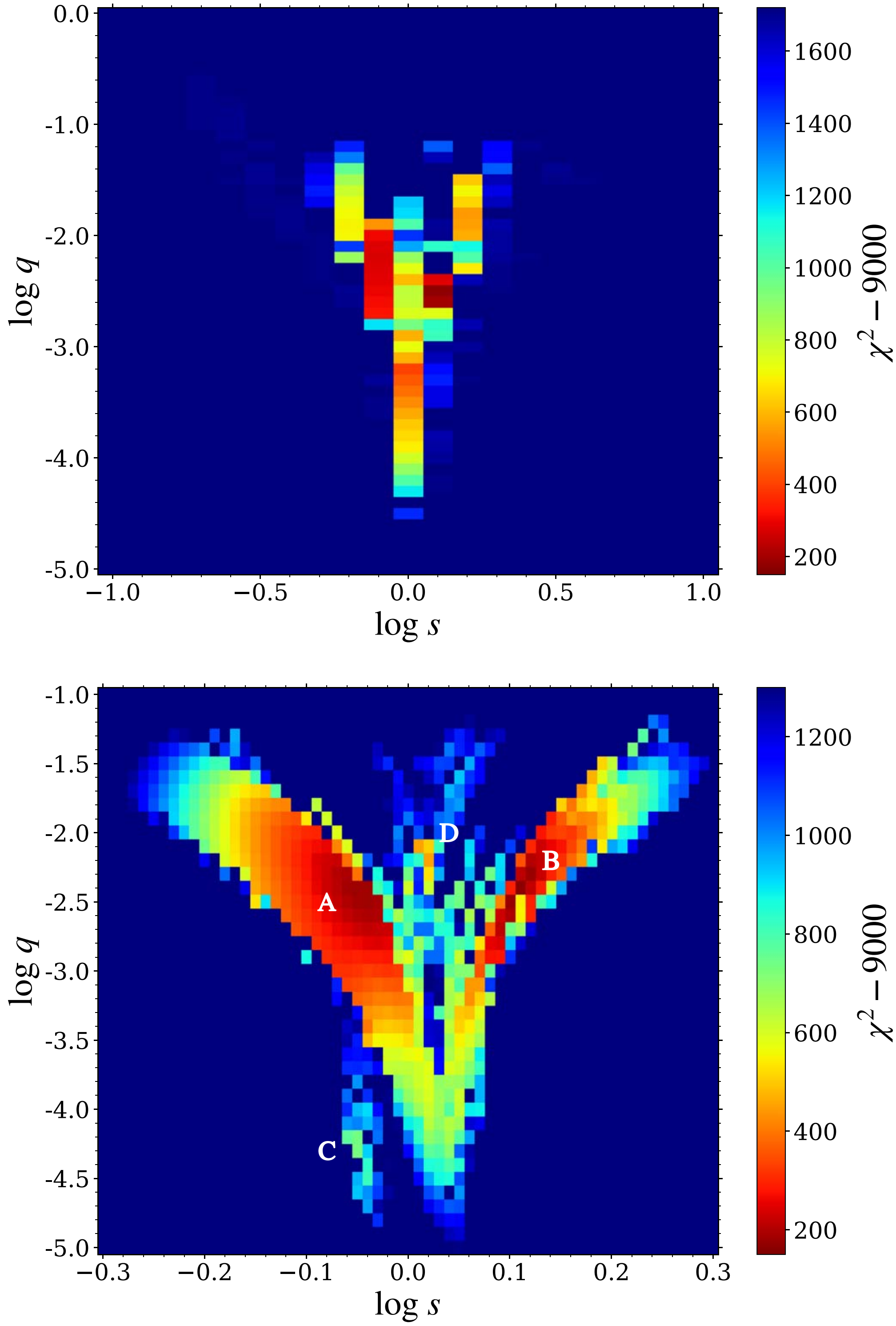

Figure 2. χ^2 surface in the ($\log s$, $\log q$) plane drawn from the grid search. The upper panel shows the space that is equally divided on a (21×51) grid with ranges of $-1.0 \leqslant \log s \leqslant 1.0$ and $-5.0 \leqslant \log q \leqslant 0$, respectively. The lower panel shows the space that is equally divided on a (61×41) grid with ranges of $-0.3 \leqslant \log s \leqslant 0.3$ and $-5.0 \leqslant \log q \leqslant -1.0$, respectively. The labels "A," "B," "C," and "D" in the lower panel show the four distinct minima.

We note that these two solutions are related by the so-called close–wide degeneracy and approximately take $s \leftrightarrow s^{-1}$ (Griest & Safizadeh 1998; Dominik 1999), so we label them by "Close" (solution B, $s < 1$) and "Wide" (solution A, $s > 1$) in the following analysis. The solutions "C" and "D" are disfavored by $\Delta\chi^2 \sim 474$ and $\Delta\chi^2 \sim 235$, respectively, so we exclude these two solutions. For both the solutions "Close" and "Wide," the data are consistent with a point-source model within a $\sim 2\sigma$ level, and the upper limit for ρ is 2.0×10^{-3} for the solution "Close" and 2.8×10^{-3} for the solution "Wide." The best-fit model curves for the two solutions are shown in Figure 1, and their magnification maps are shown in Figure 3.

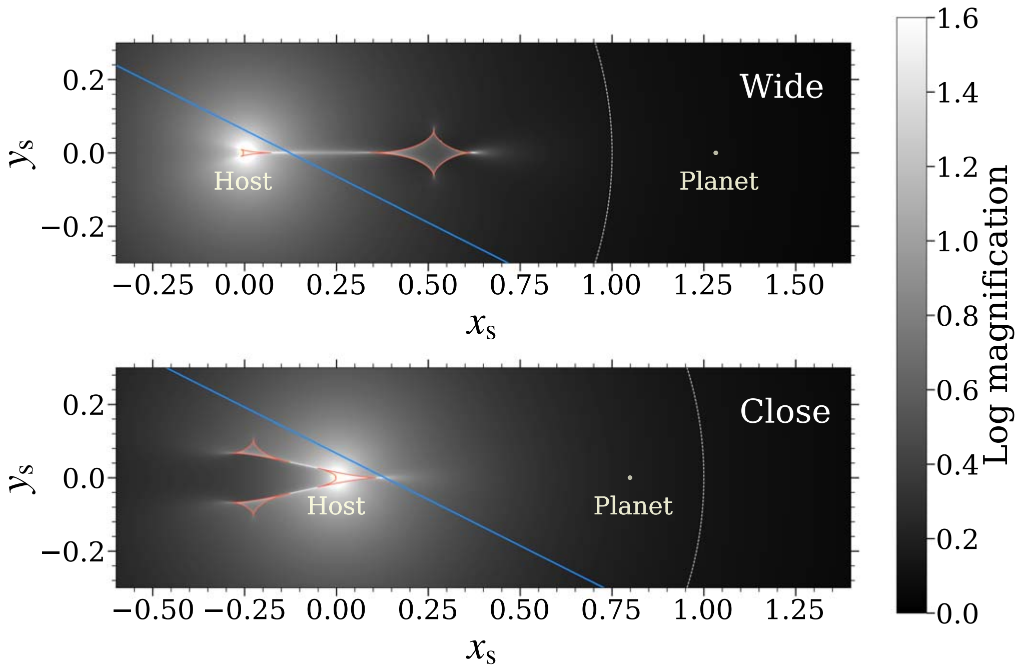

Figure 3. Magnification maps of the standard "Wide" (upper panel) and "Close" (lower panel) models shown in Table 1. In each panel, the blue line with an arrow represents the trajectory of the source with direction. The red contours are the caustics. The dashed lines indicate the Einstein ring and both x_S and y_S are in units of the Einstein radius. The gray scale indicates the magnification of a point source at each position, where white means higher magnification.

Table 1
Best-fit Parameters and Their 68% Uncertainty Range from MCMC for Four Distinct Minima Shown in Figure 2

Solutions	A	B	C	D
t_0 (HJD′)	7487.58(4)	7487.67(4)	7487.39(4)	7487.26(5)
u_0	0.062(5)	0.055(5)	0.127(13)	0.045(3)
t_E	49.9(3.4)	55.3(3.6)	30.0(2.1)	64.8(4.2)
s	0.90(2)	1.29(2)	0.89(1)	1.02(1)
q (10^{-3})	3.8(4)	4.1(5)	0.055(9)	5.7(9)
α (deg)	333.1(0.5)	333.3(0.5)	150.3(0.7)	266.3(0.8)
$\rho(10^{-3})$	<2.0	<2.8	0.8(2)	0.4(1)
I_S	22.01(5)	22.12(5)	21.46(4)	22.28(5)
I_B	18.25(1)	18.25(1)	18.26(1)	18.25(1)
χ^2/dof	9174.1/9154	9158.0/9154	9631.7/9154	9393.0/9154

Table 2
Best-fit Parameters and Their 68% Uncertainty Range for Binary-lens Model with Parallax

	Wide		Close	
Solutions	W_+	W_-	C_+	C_-
t_0 (HJD′)	7487.69(7)	7487.68(6)	7487.60(4)	7487.61(4)
u_0	0.053(5)	−0.056(4)	0.061(5)	−0.061(4)
t_E	56.2(3.9)	54.2(2.9)	50.0(3.1)	49.5(2.7)
s	1.31(3)	1.30(2)	0.89(2)	0.88(2)
q (10^{-3})	4.6(9)	4.5(8)	4.3(6)	4.4(6)
α (deg)	335.1(2.0)	25.4(1.7)	335.1(1.3)	24.7(1.1)
$\rho(10^{-3})$	<2.7	<2.7	<2.2	<2.2
$\pi_{E,N}$	0.56(0.59)	−0.46(0.56)	0.66(40)	−0.79(37)
$\pi_{E,E}$	0.08(8)	0.05(8)	0.07(10)	0.02(8)
I_S	22.14(5)	22.10(4)	22.01(5)	22.00(4)
I_B	18.25(1)	18.25(1)	18.25(1)	18.25(1)
χ^2/dof	9156.8/9152	9156.3/9152	9171.9/9152	9171.1/9152

In addition, we check whether the fit further improves by considering the microlens-parallax effect,

$$\boldsymbol{\pi}_E = \frac{\pi_{rel}}{\theta_E}\frac{\boldsymbol{\mu}_{rel}}{\mu_{rel}}, \tag{3}$$

where (π_{rel}, $\boldsymbol{\mu}_{rel}$) are the lens–source relative (parallax, proper motion), which is caused by the orbital acceleration of Earth (Gould 1992). We also fit $u_0 > 0$ and $u_0 < 0$ solutions to consider the ecliptic degeneracy (Skowron et al. 2011). To facilitate the further discussion of these solutions, we label them by $C_\pm$ or $W_\pm$. The letter stands for "Close" ($s < 1$) or "Wide" ($s > 1$), while the subscript refers to the sign of u_0. The addition of the parallax to the model does not significantly improve the fit, providing an improvement of $\Delta\chi^2 < 3.0$ for the $C_\pm$ solutions and $\Delta\chi^2 < 1.7$ for the $W_\pm$ solutions. However, we find that the east component of the parallax vector $\pi_{E,E}$ is well constrained for all the solutions, while the constraint on the north component $\pi_{E,N}$ is considerably weaker. Table 2 shows best-fit parameters of the standard binary-lens model, $C_\pm$ and $W_\pm$ solutions, and Figure 4 shows the likelihood distribution of ($\pi_{E,N}$, $\pi_{E,E}$) from MCMC.

3.2. Binary-source (1L2S) Modeling

The total magnification of a binary-source event is the superposition of two point-lens events,

$$A_\lambda = \frac{A_1 f_{1,\lambda} + A_2 f_{2,\lambda}}{f_{1,\lambda} + f_{2,\lambda}} = \frac{A_1 + q_{f,\lambda} A_2}{1 + q_{f,\lambda}}, \tag{4}$$

$$q_{f,\lambda} = \frac{f_{2,\lambda}}{f_{1,\lambda}}, \tag{5}$$

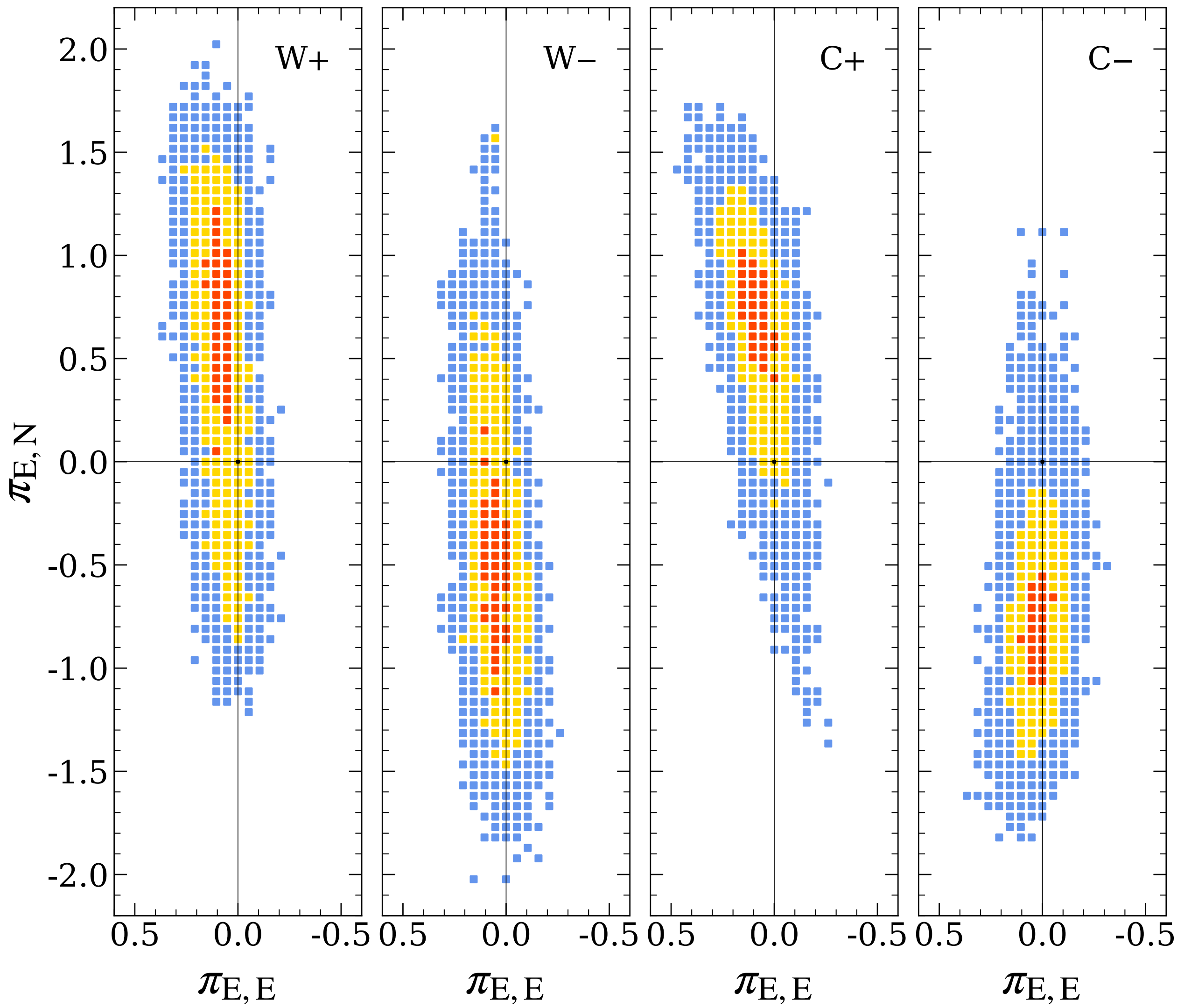

Figure 4. Likelihood distributions for π_E derived from MCMC for $W_\pm$ and $C_\pm$ solutions (see Table 1 for the solution parameters). Red, yellow, and blue show likelihood ratios $[-2\Delta \ln \mathcal{L}/\mathcal{L}_{max}] < (1, 4, \infty)$, respectively.

where $f_{i,\lambda}$ ($i = 1, 2$) is the flux at wavelength λ of each source and A_λ is total magnification. We search for 1L2S solutions using MCMC, and the best-fit model is disfavored by $\Delta\chi^2 \sim 38$ compared to the binary-lens "Wide" model (see Table 3). Figure 5 presents their cumulative distribution of χ^2 differences, which shows that the χ^2 differences are mainly from ± 20 days from the peak, rather than outliers. We also consider the microlens-parallax effect, but the improvement is very minor with $\Delta\chi^2 \sim 1.4$. Thus, we exclude the 1L2S solution.

4. Source Properties

We conduct a Bayesian analysis in Section 5 to estimate the physical parameters of the lens systems, which requires the constraints of the source properties. Thus, we estimate the angular radius θ_* and the proper motion of the source in this section.

4.1. Color–Magnitude Diagram

To further estimate the angular Einstein radius $\theta_E = \theta_*/\rho$, we estimate the angular radius θ_* of the source by locating the source on a CMD (Yoo et al. 2004). We calibrate the KMTC02 pyDIA reduction to the OGLE-III star catalog (Szymański et al. 2011) and construct a $V - I$ versus I CMD using stars within a $2' \times 2'$ square centered on the event (see Figure 6). The red

Table 3
Best-fit Parameters and Their 68% Uncertainty Range from MCMC for Binary-source Models

Solution	Standard	Parallax Models $u_0 > 0$	Parallax Models $u_0 < 0$
$t_{0,1}$ (HJD′)	7487.12(2)	7487.17(4)	7487.15(4)
$t_{0,2}$ (HJD′)	7494.73(3)	7493.78(3)	7493.77(3)
$u_{0,1}$	0.046(2)	0.048(2)	−0.046(2)
$u_{0,2}$	0.002(2)	0.002(2)	−0.002(2)
t_E (days)	65.02(3)	64.98(6)	65.02(6)
ρ_1	0.012(10)	0.017(13)	0.014(12)
ρ_2	0.0045(13)	0.0043(9)	0.0046(11)
$q_{f,I}$	0.038(3)	0.034(5)	0.037(4)
I_S	22.36(16)	22.35(14)	22.36(14)
I_B	18.25(1)	18.25(1)	18.25(1)
χ^2/dof	9196.2/9153	9194.8/9151	9194.2/9151

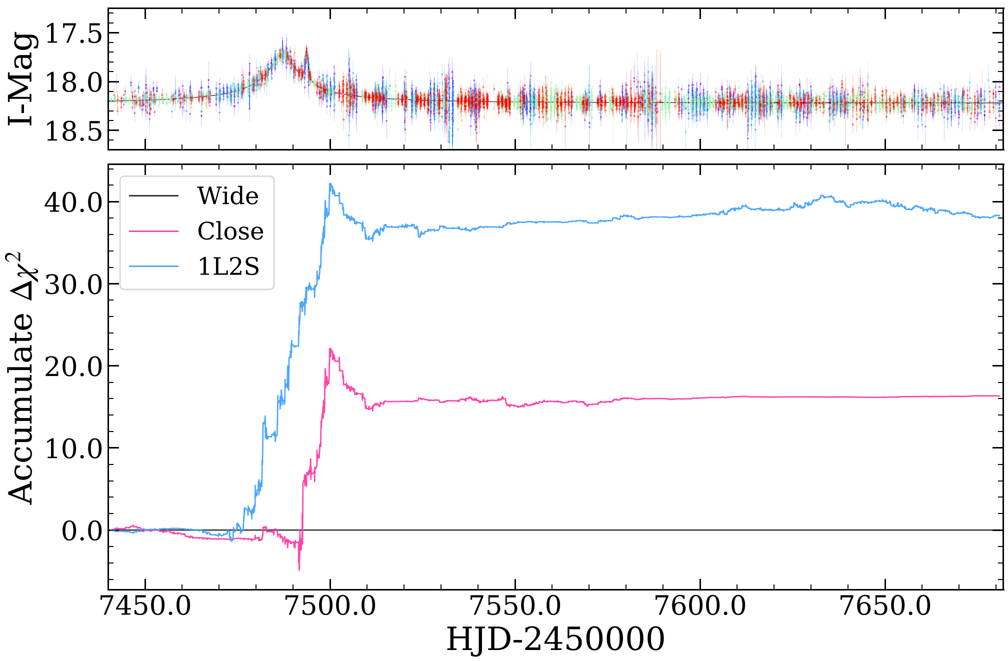

Figure 5. Cumulative distribution of χ^2 differences ($\Delta\chi^2 = \chi^2_{\rm model} - \chi^2_{\rm Wide}$) between the "Close," binary-source (1L2S), and the "Wide" models.

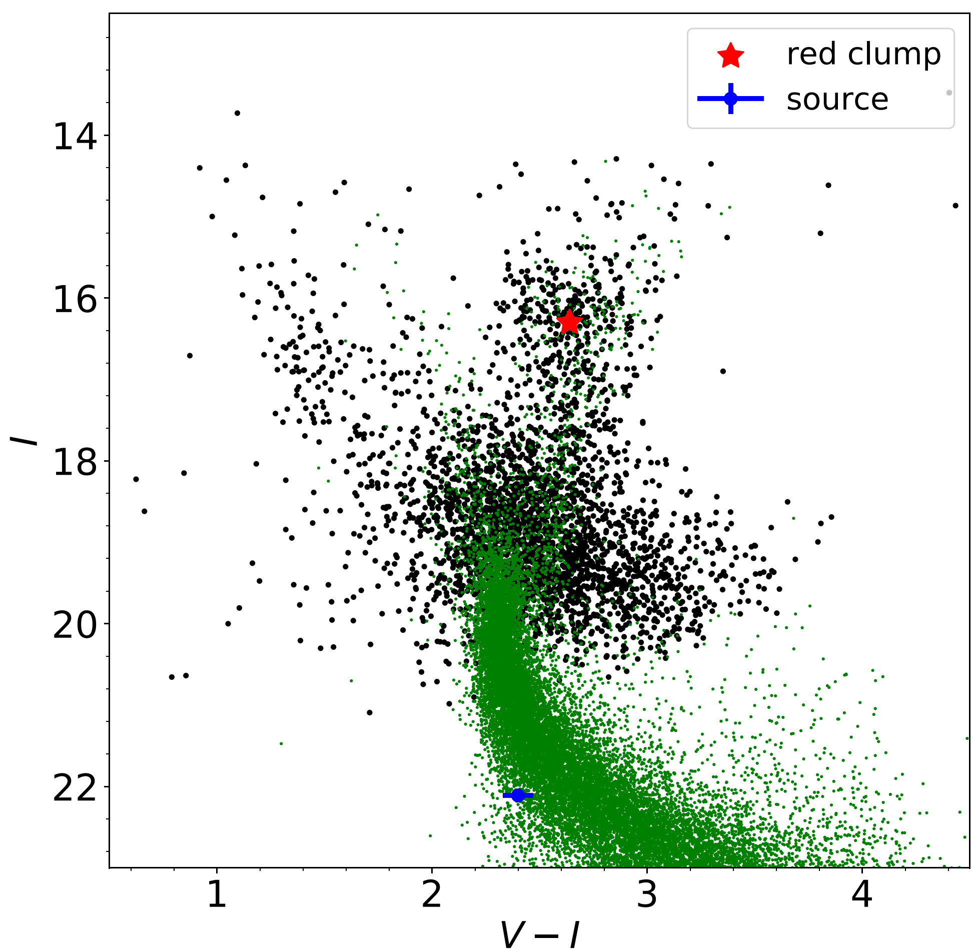

Figure 6. Color–magnitude diagram of a $2' \times 2'$ square centered on KMT-2016-BLG-1836. The black dots show the stars from pyDIA photometry of the KMTC02 data, which are calibrated to OGLE-III star catalog (Szymański et al. 2011), and the green dots show the *HST* CMD of Holtzman et al. (1998), whose red-clump centroid is adjusted to match pyDIAs using the Holtzman field red-clump centroid of $(V - I, I) = (1.62, 15.15)$ (Bennett et al. 2008). The red asterisk shows the centroid of the red clump, and the blue dot indicates the position of the source.

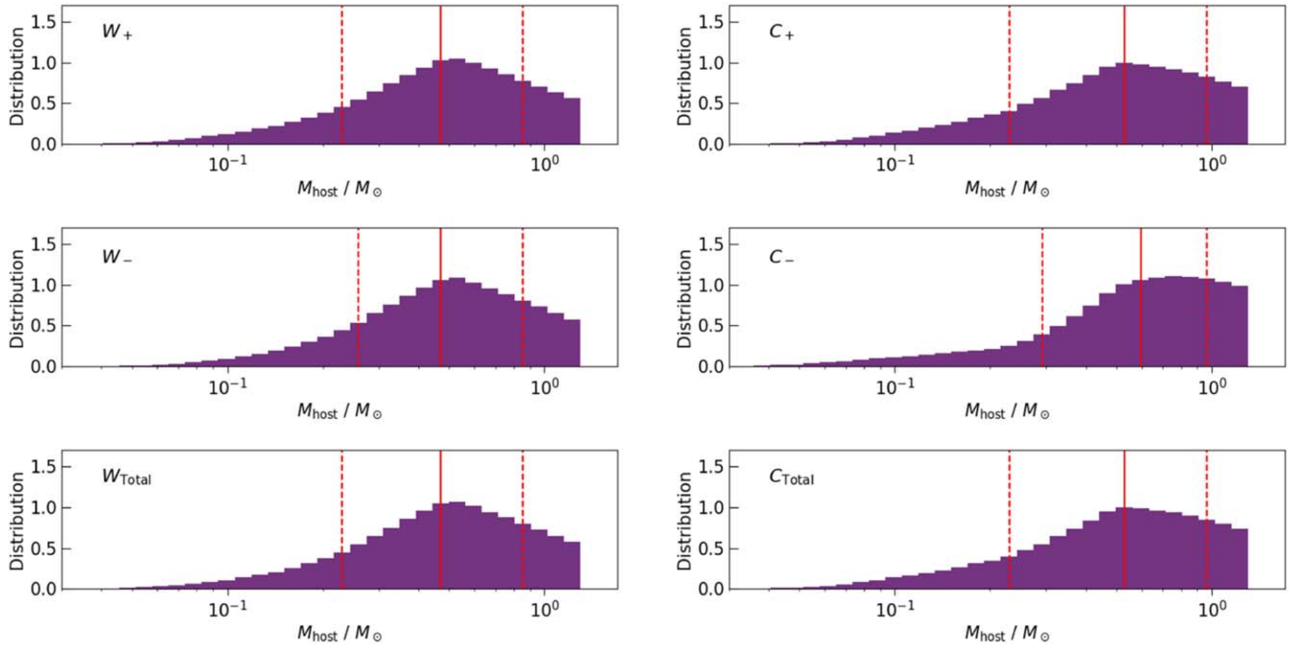

Figure 7. Bayesian posterior distributions of the lens host-mass $M_{\rm host}$ for each solution of $C_\pm$ and $W_\pm$ (top two rows) and the combined distributions for $C_\pm$ and $W_\pm$ (bottom row). In each panel, the red solid vertical line represents the median value and the two red dashed lines represent 16th and 84th percentiles of the distribution.

giant clump is at $(V-I, I)_{\rm cl} = (2.64 \pm 0.01, 16.30 \pm 0.02)$, whereas the source is at $(V-I, I)_{\rm S} = (2.40 \pm 0.07, 22.12 \pm 0.05)$ for the "Wide" solution and $(V-I, I)_{\rm S} = (2.40 \pm 0.07, 22.01 \pm 0.05)$ for the "Close" solution. We adopt the intrinsic color and dereddened magnitude of the red giant clump of $(V-I, I)_{\rm cl,0} = (1.06, 14.42)$ from Bensby et al. (2013) and Nataf et al. (2016), and then we derive the intrinsic color and dereddened brightness of the source as $(V-I, I)_{\rm S,0} = (0.82 \pm 0.08, 20.24 \pm 0.06)$ for the "Wide" solution and $(V-I, I)_{\rm S,0} = (0.82 \pm 0.08, 20.13 \pm 0.06)$ for the "Close" solution. These values suggest that the source is either a late-G or early-K type main-sequence star. Using the color/surface-brightness relation for dwarfs and subgiants of Adams et al. (2018), we obtain

$$\theta_* = 0.32 \pm 0.03 \ \ \mu\text{as for the Wide solution}, \tag{6}$$

$$\theta_* = 0.34 \pm 0.03 \ \ \mu\text{as for the Close solution}. \tag{7}$$

4.2. Source Proper Motion

For KMT-2016-BLG-1836, the microlens source is too faint to measure its proper motion either from *Gaia* (e.g., Li et al. 2019) or from ground-based data (e.g., Shvartzvald et al. 2019). However, we can still estimate the source proper motion by the proper-motion distribution of bulge stars in the *Gaia* DR2 catalog (Gaia Collaboration et al. 2016, 2018). We examine a *Gaia* CMD using the stars within 1 arcmin and derive the proper motion (in the Sun frame) of red giant branch stars ($G < 18.6$; $B_p - R_p > 2.2$). We remove one outlier and obtain (in the Sun frame)

$$\langle \boldsymbol{\mu}_{\rm bulge}(\ell, b) \rangle = (-6.0, -0.2) \pm (0.2, 0.2) \text{ mas yr}^{-1}, \tag{8}$$

$$\sigma(\boldsymbol{\mu}_{\rm bulge}) = (3.5, 3.0) \pm (0.2, 0.1) \text{ mas yr}^{-1}. \tag{9}$$

5. Lens Properties

5.1. Bayesian Analysis

For a lensing object, the total mass is related to $\theta_{\rm E}$ and $\pi_{\rm E}$ by Gould (1992, 2000)

$$M_{\rm L} = \frac{\theta_{\rm E}}{\kappa \pi_{\rm E}}, \tag{10}$$

and its distance by

$$D_{\rm L} = \frac{\rm au}{\pi_{\rm E}\theta_{\rm E} + \pi_{\rm S}}, \tag{11}$$

where $\kappa \equiv 4G/(c^2 \text{au}) = 8.144 \text{ mas}/M_\odot$, $\pi_{\rm S} = \text{au}/D_{\rm S}$ is the source parallax and $D_{\rm S}$ is the source distance. In the present case, neither $\theta_{\rm E}$ nor $\pi_{\rm E}$ are unambiguously measured, so we conduct a Bayesian analysis to estimate the physical parameters of the lens systems.

For each solution of $C_\pm$ and $W_\pm$, we first create a sample of 10^9 simulated events from the Galactic model of Zhu et al. (2017). We also choose the initial mass function of Kroupa (2001) and $1.3 M_\odot$ for the upper end of the initial mass function. The only exception is that we draw the source proper motions from a Gaussian distribution with the parameters that were derived in Section 4.2. For each simulated event i of solution k, we then weight it by

$$\omega_{{\rm Gal},i,k} = \Gamma_{i,k} \mathcal{L}_{i,k}(t_{\rm E}) \mathcal{L}_{i,k}(\boldsymbol{\pi}_{\rm E}) \mathcal{L}_{i,k}(\theta_{\rm E}), \tag{12}$$

where $\Gamma_{i,k} \propto \theta_{{\rm E},i,k} \times \mu_{{\rm rel},i,k}$ is the microlensing event rate, $\mathcal{L}_{i,k}(t_{\rm E})$, $\mathcal{L}_{i,k}(\boldsymbol{\pi}_{\rm E})$ are the likelihood of its inferred parameters $(t_{\rm E}, \boldsymbol{\pi}_{\rm E})_{i,k}$ given the error distributions of these quantities derived from the MCMC for that solution

$$\mathcal{L}_{i,k}(t_{\rm E}) = \frac{\exp[-(t_{{\rm E},i,k} - t_{{\rm E},k})^2 / 2\sigma^2_{t_{{\rm E},k}}]}{\sqrt{2\pi}\,\sigma_{t_{{\rm E},k}}}, \tag{13}$$

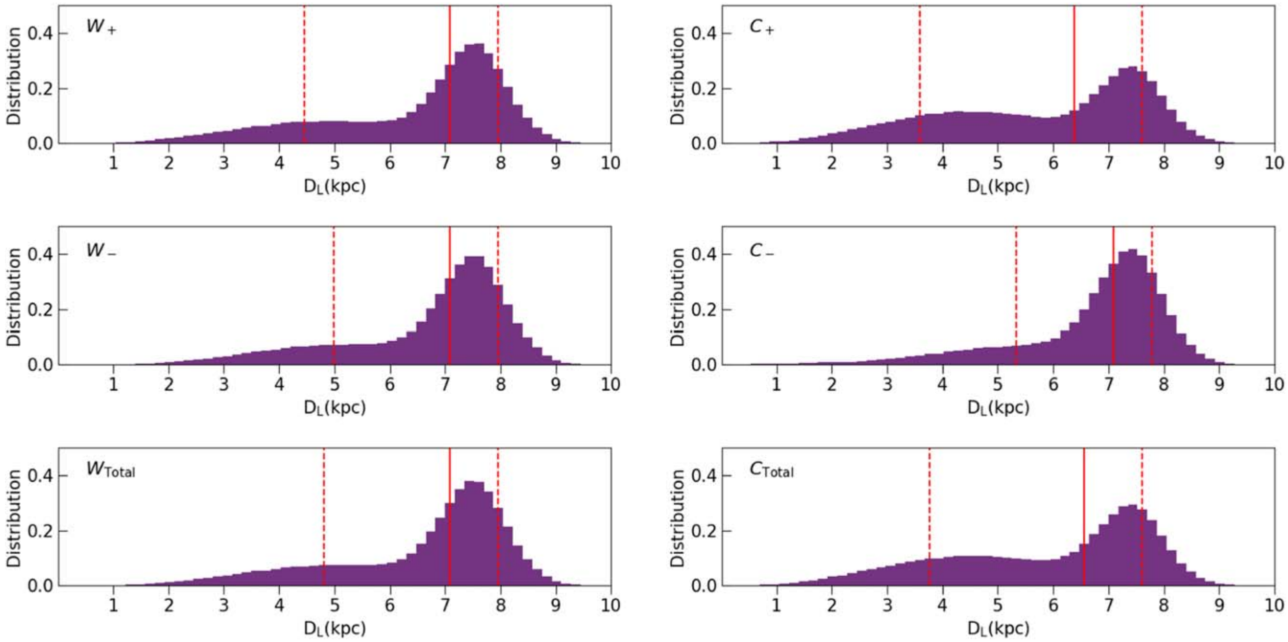

Figure 8. Bayesian posterior distributions of the lens distance $D_{\rm L}$. The plot is similar to Figure 7.

Table 4
Physical Parameters for KMT-2016-BLG-1836

Solutions	Physical Properties				Relative Weights	
	$M_{\rm host}(M_\odot)$	$M_{\rm planet}(M_{\rm J})$	$D_{\rm L}$(kpc)	$r_\perp$(au)	Gal.Mod.	χ^2
W_+	$0.48^{+0.39}_{-0.25}$	$2.2^{+1.9}_{-1.2}$	$7.1^{+0.8}_{-2.6}$	$3.6^{+1.2}_{-0.9}$	0.928	0.779
W_-	$0.49^{+0.39}_{-0.25}$	$2.2^{+1.8}_{-1.1}$	$7.2^{+0.8}_{-2.2}$	$3.5^{+1.1}_{-0.9}$	1.000	1.000
$W_{\rm Total}$	$0.49^{+0.38}_{-0.25}$	$2.2^{+1.9}_{-1.1}$	$7.1^{+0.8}_{-2.4}$	$3.5^{+1.1}_{-0.9}$	…	…
C_+	$0.51^{+0.41}_{-0.28}$	$2.2^{+1.8}_{-1.2}$	$6.3^{+1.3}_{-2.7}$	$2.7^{+0.7}_{-0.7}$	0.844	0.0004
C_-	$0.60^{+0.40}_{-0.32}$	$2.7^{+1.8}_{-1.4}$	$7.1^{+0.7}_{-1.8}$	$2.6^{+0.7}_{-0.6}$	0.247	0.0006
$C_{\rm Total}$	$0.53^{+0.42}_{-0.29}$	$2.3^{+1.9}_{-1.3}$	$6.5^{+1.2}_{-2.8}$	$2.7^{+0.7}_{-0.7}$	…	…
Total	$0.49^{+0.38}_{-0.25}$	$2.2^{+1.9}_{-1.1}$	$7.1^{+0.8}_{-2.4}$	$3.5^{+1.1}_{-0.9}$	…	…

$$\mathcal{L}_{i,k}(\boldsymbol{\pi}_{\rm E}) = \frac{\exp[-\sum_{m,n=1}^{2} b^k_{m,n}(\pi_{{\rm E},m,i} - \pi_{{\rm E},m,k})(\pi_{{\rm E},n,i} - \pi_{{\rm E},n,k})/2]}{2\pi/\sqrt{\det b^k}}, \tag{14}$$

$b^k_{m,n}$ is the inverse covariance matrix of $\boldsymbol{\pi}_{{\rm E},k}$, (m, n) are dummy variables ranging over (N, E), and $\mathcal{L}_{i,k}(\theta_{\rm E})$ is the likelihood derived from the minimum χ^2 for the lower envelope of the (χ^2 versus ρ) diagram from MCMC and the measured source angular radius θ_* from Section 4.1. Finally, we weight each solution by $\exp(-\Delta\chi^2_k/2)$, where $\Delta\chi^2_k$ is the χ^2 difference between the kth solution and the best-fit solution.

Table 4 shows the resulting lens properties and relative weights for each solution and the combined results. We find that the "Wide" solutions are significantly favored because they are preferred by a factor of $\sim\exp(14/2) \sim 10^3$ from the χ^2 weight, while the "Wide" solutions also have a slightly higher Galactic model likelihood. The net effect is that the resulting combined solution is basically the same as the "Wide" solution. The Bayesian analysis yields a host mass of $M_{\rm host} = 0.49^{+0.38}_{-0.25}\,M_\odot$, a planet mass of $M_{\rm planet} = 2.2^{+1.9}_{-1.1}\,M_{\rm J}$, and a host–planet projected separation of $r_\perp = 3.5^{+1.1}_{-0.9}$ au, which indicates the planet is a super-Jovian planet well beyond the snow line of an M/K dwarf star (assuming a snow-line radius of $r_{\rm SL} = 2.7(M/M_\odot)$ au; Kennedy & Kenyon 2008). For each solution, the resulting distributions of the lens host-mass $M_{\rm host}$ and the lens distance $D_{\rm L}$ are shown in Figures 7 and 8, respectively. The resulting combined distributions of the lens properties are shown in Figure 9.

5.2. Blended Light

The light-curve analysis shows that the blended light for the pySIS light curve is $I_{\rm B} \sim 18.25$. To investigate the blend, we check the higher-resolution i-band images (pixel scale $0''.185$, FWHM $\sim 0''.6$) taken from the Canada–France–Hawaii

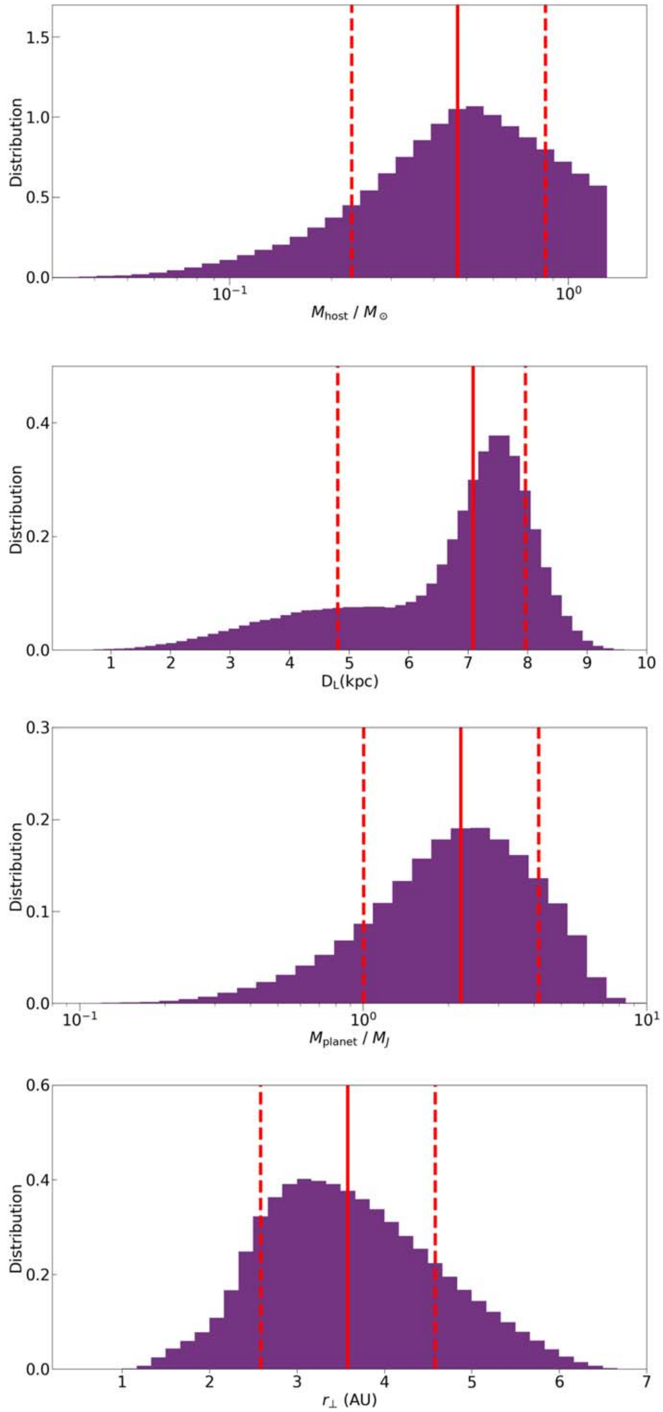

Figure 9. Combined Bayesian distributions of the lens host-mass $M_{\rm host}$, the lens distance $D_{\rm L}$, the planet-mass $M_{\rm planet}$, and the projected separation $r_\perp$ of the planet.

Telescope (CFHT) located at the Maunakea Observatories in 2018 (Zang et al. 2018b). We identify the source position in the CFHT images from an astrometric transformation of the highly magnified KMTC02 images. We use DoPhot (Schechter et al. 1993) to identify nearby stars and do photometry. As a result, DoPhot identifies two stars within $1''$ (see Figure 10): an $I = 18.18 \pm 0.02$ star offset from the source by $0\rlap{.}''88$ and an $I = 19.43 \pm 0.05$ star offset by $0\rlap{.}''61$. Thus, the blend of the pySIS light curve is from unrelated ambient stars. In addition, the total brightness of the source and the lens is fainter than the nearby $I = 19.43 \pm 0.05$ star.

From the CMD analysis and the Bayesian analysis, the source is a late-G or early-K dwarf and the lens is probably an M/K dwarf. Thus, the lens and source may have approximately equal brightness in the near-infrared, therefore follow-up adaptive optics (AO) observations can potentially strongly constrain the lens brightness and thus the mass and distance of the planetary system (Batista et al. 2015; Bennett et al. 2015; Bhattacharya et al. 2018). In addition, our Bayesian analysis shows that the lens–source relative proper motion is $\mu_{\rm rel} = 3.3^{+1.5}_{-0.9}$mas yr^{-1}, so the lens and source will be separated by about 40 mas by 2028. Thus, the source and lens can be resolved by the first AO light on next-generation (30 m) telescopes, which have a resolution of $\theta \sim 14(D/30\ {\rm m})^{-1}$ mas in the H band.

6. Discussion

We have reported the discovery and analysis of the microlens planet KMT-2016-BLG-1836Lb, for which the $\sim$1 day, $q \sim 0.004$ planetary perturbation was detected and characterized by the $\Gamma \sim 4\ {\rm hr}^{-1}$ observations of KMTNet. Many previous works have explored the mass-ratio distribution of microlens planets. Of particular note is the work of Suzuki et al. (2016), which discovered a break in the mass-ratio function of planets at $\log q \sim -4$. In addition, Mróz et al. (2017) tested whether observation strategy (survey versus survey + follow-up) could affect the observed mass-ratio distribution. A full analysis of the mass-ratio distribution for KMTNet planets is well beyond the scope of this work. However, we construct an initial distribution to emphasize the need for such a detailed analysis in the future.

We conduct our analysis on published KMTNet planets discovered in the 2016–2018 seasons and also on the 2016 season alone, since the 2016 season is the most likely to be complete, i.e., have the least publication bias. Including KMT-2016-BLG-1836Lb, there are 13 published microlens planets with KMTNet data from 2016 and 31 published planets from 2016 to 2018, most of which (19/31 for all the planets from 2016 to 2018, and 8/13 for planets from 2016) are located in the $\Gamma > 1\ {\rm hr}^{-1}$ fields of KMTNet.[20] The upper and lower panels of Figure 11 show the cumulative distributions of planets by log mass-ratio $\log q$ for 31 planets from 2016 to 2018 and 13 planets from 2016, respectively. For each panel, we also show the cumulative distributions of $\log q$ for planets observed at cadences of $\Gamma > 1\ {\rm hr}^{-1}$ and $\Gamma \leqslant 1\ {\rm hr}^{-1}$. For events with n degenerate solutions, each of the solutions are included at a weight of $1/n$.

The KMTNet planet sample appears to have a mass-ratio desert at $-3.7 \lesssim \log\ q \lesssim -3.0$. The only planet ($\log q \sim -3.2$) that appears in this desert is one of the two degenerate solutions for OGLE-2017-BLG-0373Lb. This potential mass-ratio desert cannot be caused by the detection efficiency of KMTNet because eight planets with $\log q < -3.7$ have been detected by $\Gamma > 1\ {\rm hr}^{-1}$. However, the sample of planets from Suzuki et al. (2016), which was subject to a rigorous analysis, does not show any evidence for a mass-ratio desert in this range. Likewise, Mróz et al. (2017) found that the cumulative distributions of $\log q$ are nearly uniformly distributed in

[20] Actually, only OGLE-2018-BLG-0596Lb was observed at a cadence of $\Gamma \sim 2\ {\rm hr}^{-1}$, while other planets were observed at cadences of $\Gamma \geqslant 4\ {\rm hr}^{-1}$.

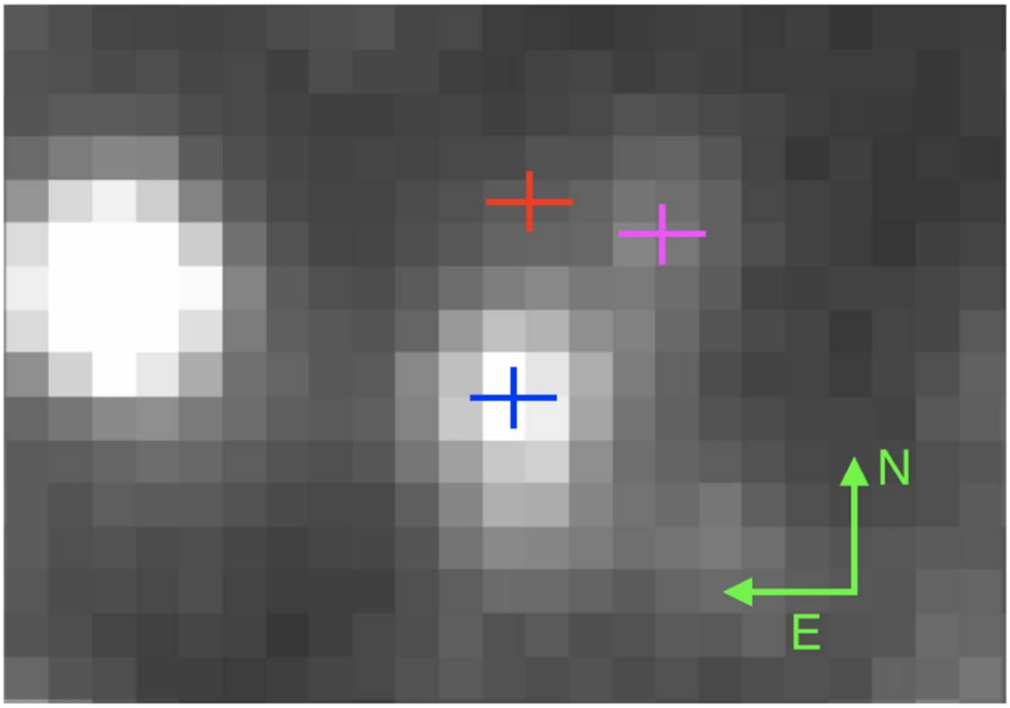

Figure 10. *i*-band CFHT images within $4\farcs9 \times 3\farcs0$ around the event. The red cross indicates the source position derived from an astrometric transformation of the highly magnified KMTC02 images. The blue and magenta crosses indicate the $I = 18.18 \pm 0.02$ star and $I = 19.43 \pm 0.05$ star found by DoPhot (Schechter et al. 1993), respectively.

$-4.3 < \log q < -2.0$ (i.e., constant number of detections in each bin of equal $\log q$) for a sample including 44 published microlensing planets before 2016 plus OGLE-2016-BLG-0596Lb.

The most likely source of this discrepancy is incompleteness due to publication bias. For example, the number of planets with $\log q$ ($< -3.7, > -3.7$) are (2, 11) in 2016, (4, 5) in 2017, and (3, 6) in 2018, which suggests that there are likely be some unpublished planets with $\log q > -3.7$ from 2017 and 2018. This publication bias could result in the missing planets at $-3.7 \lesssim \log q \lesssim -3.0$ and thus the apparent mass-ratio desert.

The core accretion runaway growth scenario predicts that the planets in the mass range of 30–100$M_\oplus$ are rare (Ida & Lin 2004). For the typical microlensing lens mass of $M_{\rm host} \sim 0.3$–0.5 $M_\odot$, 30–100$M_\oplus$ corresponds to the mass ratio $-3.7 \lesssim \log q \lesssim -3.0$. Thus, the mass-ratio distribution from microlensing can be used to test predictions of the core accretion theory. Suzuki et al. (2018) found that the mass-ratio distribution from Suzuki et al. (2016) is inconsistent with those predictions. KMTNet enables an independent measurement of this mass-ratio distribution. If the potential mass-ratio desert of the KMTNet planet sample is real, it could be consistent with the core accretion theory of planet formation and potentially contradicts Suzuki et al. (2018). Verifying this apparent mass-ratio desert requires a full statistical analysis of the KMTNet data including detection efficiency and selection biases.

This research has made use of the KMTNet system operated by the Korea Astronomy and Space Science Institute (KASI) and the data were obtained at three host sites of CTIO in Chile, SAAO in South Africa, and SSO in Australia. This research uses data obtained through the Telescope Access Program (TAP), which has been funded by the National Astronomical Observatories of China, the Chinese Academy of Sciences, and the Special Fund for Astronomy from the Ministry of Finance. H.Y., X.Z., W.Z., W.T., and S.M. acknowledge support by the National Science Foundation of China (grant No. 11821303 and 11761131004). Work by A.G. was supported by AST-1516842 and by JPL grant 1500811. A.G. received support from the European Research Council under the European Unions Seventh Framework Programme (FP 7) ERC Grant Agreement No. [321035]. Work by C.H. was supported by the grant (2017R1A4A1015178) of National Research Foundation of Korea. Work by P.F. and W.Z. was supported by Canada–France–Hawaii Telescope (CFHT). M.T.P. was supported by NASA grants NNX14AF63G and NNG16PJ32C, as well as the Thomas Jefferson Chair for Discovery and Space Exploration. W.Z. was supported by the Beatrice and Vincent Tremaine Fellowship at CITA. Partly based on observations obtained with MegaPrime/MegaCam, a joint project of CFHT and CEA/DAPNIA, at the Canada–France–Hawaii Telescope (CFHT), which is operated by the National Research Council (NRC) of Canada, the Institut National des Science de lUnivers of the Centre National de la Recherche Scientifique (CNRS) of France, and the University of Hawaii.

Software: pySIS (Albrow et al. 2009), pyDIA (Albrow 2017, as developed on GitHub), emcee (Foreman-Mackey et al. 2013), DoPhot (Schechter et al. 1993).

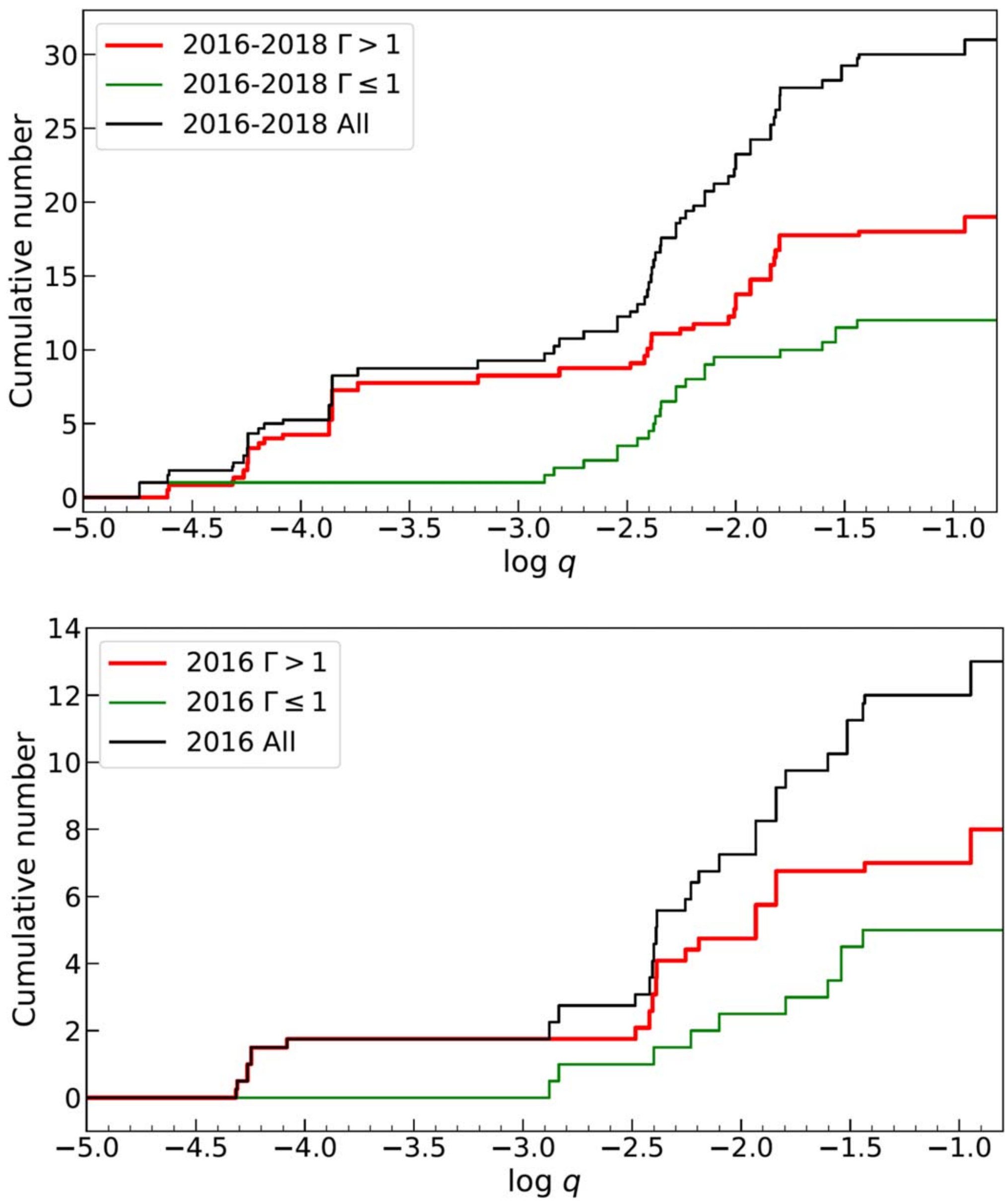

Figure 11. Cumulative distributions of 31 published KMTNet microlensing planets from 2016 to 2018 by log q (upper panel) and 13 published KMTNet microlensing planets from 2016 by log q (lower panel). In each panel, the red and green lines represent the distributions for planets observed at cadences of $\Gamma > 1\ \mathrm{hr}^{-1}$, $\Gamma \leqslant 1\ \mathrm{hr}^{-1}$, respectively, and the black line represents the distribution of all the planets.

ORCID iDs

Hongjing Yang https://orcid.org/0000-0003-0626-8465
Kyu-Ha Hwang https://orcid.org/0000-0002-9241-4117
Weicheng Zang https://orcid.org/0000-0001-6000-3463
Shude Mao https://orcid.org/0000-0001-8317-2788
Michael D. Albrow https://orcid.org/0000-0003-3316-4012
Sun-Ju Chung https://orcid.org/0000-0001-6285-4528
Cheongho Han https://orcid.org/0000-0002-2641-9964
Youn Kil Jung https://orcid.org/0000-0002-0314-6000
In-Gu Shin https://orcid.org/0000-0002-4355-9838
Yossi Shvartzvald https://orcid.org/0000-0003-1525-5041
Jennifer C. Yee https://orcid.org/0000-0001-9481-7123
Wei Zhu https://orcid.org/0000-0003-4027-4711
Matthew T. Penny https://orcid.org/0000-0001-7506-5640
Richard W. Pogge https://orcid.org/0000-0003-1435-3053

References

Adams, A. D., Boyajian, T. S., & von Braun, K. 2018, MNRAS, 473, 3608
Alard, C., & Lupton, R. H. 1998, ApJ, 503, 325
Albrow, M. D. 2017, pyDIA: Initial release, Zenodo, doi:10.5281/zenodo.268049
Albrow, M. D., Horne, K., Bramich, D. M., et al. 2009, MNRAS, 397, 2099
Batista, V., Beaulieu, J.-P., Bennett, D. P., et al. 2015, ApJ, 808, 170
Bennett, D. P., Bhattacharya, A., Anderson, J., et al. 2015, ApJ, 808, 169
Bennett, D. P., Bond, I. A., Udalski, A., et al. 2008, ApJ, 684, 663
Bensby, T., Yee, J. C., Feltzing, S., et al. 2013, A&A, 549, A147
Bhattacharya, A., Beaulieu, J. P., Bennett, D. P., et al. 2018, AJ, 156, 289
Bond, I. A., Udalski, A., Jaroszyński, M., et al. 2004, ApJL, 606, L155
Calchi Novati, S., Gould, A., Udalski, A., et al. 2015, ApJ, 804, 20
Calchi Novati, S., Skowron, J., Jung, Y. K., et al. 2018, AJ, 155, 261
Calchi Novati, S., Suzuki, D., Udalski, A., et al. 2019, AJ, 157, 121
Dominik, M. 1999, A&A, 349, 108
Foreman-Mackey, D., Hogg, D. W., Lang, D., & Goodman, J. 2013, PASP, 125, 306

Gaia Collaboration, Brown, A. G. A., Vallenari, A., et al. 2018, A&A, 616, A1
Gaia Collaboration, Prusti, T., de Bruijne, J. H. J., et al. 2016, A&A, 595, A1
Gaudi, B. S. 1998, ApJ, 506, 533
Gould, A. 1992, ApJ, 392, 442
Gould, A. 2000, ApJ, 542, 785
Gould, A., Carey, S., & Yee, J. 2013, Spitzer Proposal, 10036
Gould, A., Carey, S., & Yee, J. 2014, Spitzer Proposal, 11006
Gould, A., Carey, S., & Yee, J. 2016, Spitzer Proposal, 13005
Gould, A., & Horne, K. 2013, ApJL, 779, L28
Gould, A., & Loeb, A. 1992, ApJ, 396, 104
Gould, A., Ryu, Y.-H., Calchi Novati, S., et al. 2019, arXiv:1906.11183
Gould, A., Yee, J., & Carey, S. 2015a, Spitzer Proposal, 12013
Gould, A., Yee, J., & Carey, S. 2015b, Spitzer Proposal, 12015
Gould, A., Yee, J., Carey, S., & Shvartzvald, Y. 2018, Spitzer Proposal, 14012
Griest, K., & Safizadeh, N. 1998, ApJ, 500, 37
Han, C. 2002, ApJ, 564, 1015
Han, C., Bennett, D. P., Udalski, A., et al. 2019a, AJ, 158, 114
Han, C., Bond, I. A., Gould, A., et al. 2018a, AJ, 156, 226
Han, C., Hirao, Y., Udalski, A., et al. 2018b, AJ, 155, 211
Han, C., Lee, C.-U., Udalski, A., et al. 2020, AJ, 159, 48
Han, C., Udalski, A., Gould, A., et al. 2017a, AJ, 154, 133
Han, C., Udalski, A., Gould, A., et al. 2017b, AJ, 154, 223
Han, C., Udalski, A., Gould, A., et al. 2019b, arXiv:1911.11953
Han, C., Yee, J. C., Udalski, A., et al. 2019c, AJ, 158, 102
Henderson, C. B., Gaudi, B. S., Han, C., et al. 2014, ApJ, 794, 52
Henderson, C. B., Poleski, R., Penny, M., et al. 2016, PASP, 128, 124401
Holtzman, J. A., Watson, A. M., Baum, W. A., et al. 1998, AJ, 115, 1946
Hwang, K. H., Kim, H. W., Kim, D. J., et al. 2018a, JKAS, 51, 197
Hwang, K.-H., Ryu, Y.-H., Kim, H.-W., et al. 2019, AJ, 157, 23
Hwang, K.-H., Udalski, A., Shvartzvald, Y., et al. 2018b, AJ, 155, 20
Ida, S., & Lin, D. N. C. 2004, ApJ, 604, 388
Jung, Y. K., Gould, A., Udalski, A., et al. 2019a, AJ, 158, 28
Jung, Y. K., Gould, A., Zang, W., et al. 2019b, AJ, 157, 72
Jung, Y. K., Hwang, K.-H., Ryu, Y.-H., et al. 2018a, AJ, 156, 208
Jung, Y. K., Udalski, A., Gould, A., et al. 2018b, AJ, 155, 219
Kennedy, G. M., & Kenyon, S. J. 2008, ApJ, 673, 502
Kim, D.-J., Kim, H.-W., Hwang, K.-H., et al. 2018a, AJ, 155, 76
Kim, H.-W., Hwang, K.-H., Kim, D.-J., et al. 2018b, arXiv:1804.03352
Kim, H.-W., Hwang, K.-H., Kim, D.-J., et al. 2018c, AJ, 155, 186
Kim, S.-L., Lee, C.-U., Park, B.-G., et al. 2016, JKAS, 49, 37
Kroupa, P. 2001, MNRAS, 322, 231
Li, S. S., Zang, W., Udalski, A., et al. 2019, MNRAS, 488, 3308
Mao, S., & Paczynski, B. 1991, ApJL, 374, L37
Mróz, P., Han, C., Udalski, A., et al. 2017, AJ, 153, 143
Mróz, P., Udalski, A., Skowron, J., et al. 2019, ApJS, 244, 29
Nataf, D. M., Gonzalez, O. A., Casagrande, L., et al. 2016, MNRAS, 456, 2692
Paczyński, B. 1986, ApJ, 304, 1
Ryu, Y.-H., Hwang, K.-H., Gould, A., et al. 2019a, AJ, 158, 151
Ryu, Y.-H., Navarro, M. G., Gould, A., et al. 2020, AJ, 159, 58
Ryu, Y.-H., Udalski, A., Yee, J. C., et al. 2019b, arXiv:1905.08148
Ryu, Y.-H., Yee, J. C., Udalski, A., et al. 2018, AJ, 155, 40
Schechter, P. L., Mateo, M., & Saha, A. 1993, PASP, 105, 1342
Shin, I. G., Ryu, Y. H., Yee, J. C., et al. 2019, AJ, 157, 146
Shvartzvald, Y., Yee, J. C., Calchi Novati, S., et al. 2017, ApJL, 840, L3
Shvartzvald, Y., Yee, J. C., Skowron, J., et al. 2019, AJ, 157, 106
Skowron, J., Ryu, Y.-H., Hwang, K.-H., et al. 2018, AcA, 68, 43
Skowron, J., Udalski, A., Gould, A., et al. 2011, ApJ, 738, 87
Street, R. A., Udalski, A., Calchi Novati, S., et al. 2016, ApJ, 819, 93
Sumi, T., Bennett, D. P., Bond, I. A., et al. 2013, ApJ, 778, 150
Suzuki, D., Bennett, D. P., Ida, S., et al. 2018, ApJL, 869, L34
Suzuki, D., Bennett, D. P., Sumi, T., et al. 2016, ApJ, 833, 145
Szymański, M. K., Udalski, A., Soszyński, I., et al. 2011, AcA, 61, 83
Udalski, A., Jaroszyński, M., Paczyński, B., et al. 2005, ApJL, 628, L109
Udalski, A., Ryu, Y.-H., Sajadian, S., et al. 2018, AcA, 68, 1
Yoo, J., DePoy, D. L., Gal-Yam, A., et al. 2004, ApJ, 603, 139
Zang, W., Hwang, K.-H., Kim, H.-W., et al. 2018a, AJ, 156, 236
Zang, W., Penny, M. T., Zhu, W., et al. 2018b, PASP, 130, 104401
Zhu, W., Udalski, A., Calchi Novati, S., et al. 2017, AJ, 154, 210